Resonant scattering in the Perseus Cluster: spectral model for constraining gas motions with *Astro-H*

I. Zhuravleva[1,2,3⋆], E. Churazov[3,4], R. Sunyaev[3,4], S. Sazonov[4,5], S. W. Allen[1,2,6], N. Werner[1,2], A. Simionescu[1,2,7], S. Konami[8], T. Ohashi[8]

[1] *Kavli Institute for Particle Astrophysics and Cosmology, Stanford University, 452 Lomita Mall, Stanford, CA 94305-4085, USA*
[2] *Department of Physics, Stanford University, 382 Via Pueblo Mall, Stanford, CA 94305-4060, USA*
[3] *MPI für Astrophysik, Karl-Schwarzschild str. 1, Garching, 85741, Germany*
[4] *Space Research Institute, Profsoyuznaya str. 84/32, Moscow, 117997, Russia*
[5] *Moscow Institute of Physics and Technology, Institutsky per. 9, 141700 Dolgoprudny, Russia*
[6] *SLAC National Accelerator Laboratory, 2575 Sand Hill Road, Menlo Park, CA 94025, USA*
[7] *Institute of Space and Astronautical Science (ISAS), JAXA, 3-1-1 Yoshinodai, Chuo-ku, Sagamihara, Kanagawa 252-5210, Japan*
[8] *Department of Physics, Tokyo Metropolitan University, 1-1 Minami-Osawa, Hachioji, Tokyo 192-0397, Japan*

ABSTRACT

X-ray spectra from cores of galaxy clusters can be strongly distorted by resonant scattering of line photons, affecting metal abundance and gas velocity measurements. We introduce simulated spectral models that take into account the resonant scattering effect, radial variations of thermodynamic properties of the hot gas, projection effects and small-scale isotropic gas motions. The key feature of the models is that all these effects are treated self-consistently for the whole spectrum, rather than for individual lines. The model spectra are publicly available and can be used for direct comparison with observed projected spectra. Comparison with the existing *XMM-Newton* and *Chandra* data of the Perseus Cluster shows that even though there is no strong evidence for the resonant scattering in Perseus, the low energy resolution of the X-ray CCDs is not sufficient to robustly distinguish spectral distortions due to the resonant scattering, different metal abundance profiles and different levels of gas turbulence. Future *Astro-H* data will resolve most of the problems we are facing with CCDs. With the help of our models, the resonant scattering analysis can be done self-consistently using the whole spectral information, constraining the level of gas turbulence already with a 100 ks observation with *Astro-H*.

Key words: line: formation - line: profiles - radiative transfer - scattering - turbulence - methods: numerical - galaxies: clusters: intracluster medium - X-rays: galaxies: clusters

1 INTRODUCTION

The scattering of photons of optically thick lines, so-called resonant scattering (hereafter RS), is important in a variety of astrophysical conditions (see e.g., Churazov et al. 2010, for a review). In the context of hot plasma in galaxy clusters the RS effect was first considered by Gilfanov, Syunyaev, & Churazov (1987). They showed that even though clusters are transparent in their thermal continua, the optical depth τ in some resonant X-ray lines can be of the order of few. Scattering of photons in the optically thick lines significantly

distorts both the radial surface brightness profile and the shape of the lines.

Distortions in spectra and intensity due to the RS effect are less prominent if turbulent motions of gas are present. Therefore, by measuring the level of line flux suppression in the optically thick lines, one can constrain the velocity amplitude of motions. This idea has been studied with radiative transfer simulations (see e.g. Shigeyama 1998; Churazov et al. 2004). It has been shown that the scattering also produces polarization of the same lines (Sazonov, Churazov, & Sunyaev 2002) in the X-ray spectra of galaxy clusters, which provides a unique way to probe gas motions perpendicular to the line of sight (Zhuravleva et al. 2010).

⋆ zhur@stanford.edu
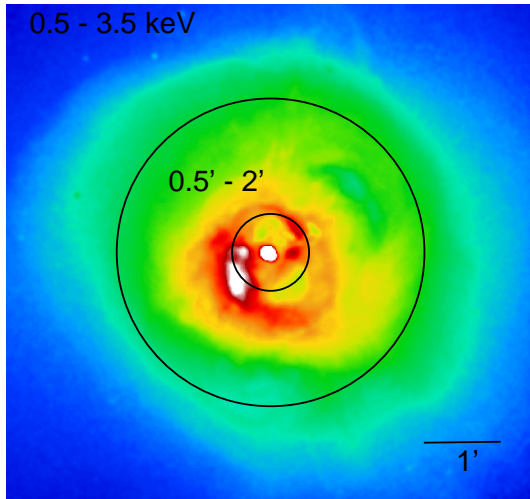
Figure 1. *Chandra* image of the central region of the Perseus Cluster in 0.5-3.5 keV energy band. The image is slightly smoothed with a 3 arcsec Gaussian. The annulus 0.5-2 arcmin is indicated. This annulus is chosen to show results of resonant scattering effect in the cluster.

Detection of the RS is difficult with the current generation of X-ray observatories due to the limited energy resolution of CCDs. For instance, several attempts have been made to detect the RS signal in the Perseus Cluster using the 6.7 keV line of the He-like iron (Molendi et al. 1998; Akimoto et al. 1999; Churazov et al. 2004; Gastaldello & Molendi 2004; Ezawa et al. 2001; Dupke & Arnaud 2001; Sanders et al. 2004). These studies revealed no strong evidence for the RS in the data. However, the spectral lines are unresolved, and uncertainties in the metal abundance profiles and projection effects complicate firm conclusions on the level of turbulence.

At lower energies ($\sim$ 0.5-2.5 keV), a better energy resolution can be reached using the Reflection Grating Spectrometer (RGS) measurements on *XMM-Newton*. The spatial extent of the cooling core of the Perseus Cluster prevents any meaningful observational constraints on the velocity broadening of spectral lines using RGS. However, the RGS measurements have been used to place constraints on turbulence in more compact cores of elliptical galaxies and cool-core clusters by measuring directly the width of individual lines (mostly upper limits, see e.g. Sanders, Fabian, & Smith 2011; Sanders & Fabian 2013; Bulbul et al. 2012) and by using the RS analysis in the Ne-like FeXVII at 15Å and 17Å (see e.g. Xu et al. 2002; Kahn et al. 2003; Werner et al. 2009; de Plaa et al. 2012). These studies found gas velocities (or upper limits) at the level of few 100 km/s. Although these lines are detected in the core of the Perseus Cluster, they are weak, and the emission in the lines is associated with the extended and complex network of filaments, which would be impossible to model realistically for the RS studies.

To date the RS analysis has been based on comparisons of fluxes in optically thick and thin lines. However, *Astro-H* will soon provide data with the energy resolution $\sim$ 5 eV, allowing us for the first time to resolve many individual lines in the spectra of galaxy clusters. Not only the line suppression can be detected, but also the modification of the line shape induced by the RS. This will push the RS analyses to a new level of precision and make the constraints on the turbulent velocities more robust.

The best way to study the RS is to fit the complete set of observed data with spectral models that take into account projection effects, line broadening due to thermal and turbulent motions of gas, and distortions in the line shape and flux due to scattering. Here, we introduce simulations that produce such models. Using emissivities in lines and continuum from detailed models of the optically thin plasmas, we calculate the RS effect within given energy bands using a Monte Carlo approach, producing projected model spectra in the format of XSPEC models (Arnaud 1996). The models take into account radial variations of density, temperature and abundance of heavy elements, partially solving the problem of the presence of multi-temperature (in projection) plasma components. The models are produced assuming different levels of turbulence. Using these models, analysis of the RS effect within given energy band can be done simultaneously and self-consistently, taking into account all lines in the spectra. To illustrate the application of our spectral models, we use available observations of the Perseus Cluster. We also discuss future application of the models to high spectral resolution data from *Astro-H*.

The structure of the paper is as follows. The data analysis and a 3D model of the Perseus Cluster are described in Section 2. Our radiative transfer simulations are presented in Section 3. Examples of our spectral models that account for the RS, projection effects and gas turbulence, are shown in Section 4.1. Application of these models on existing data, and to future data from *Astro-H* are discussed in Sections 4.2 and 4.3 respectively. Our conclusions are summarized in Section 5.

2   X-RAY DATA ANALYSIS AND PARAMETERIZATION OF THE PERSEUS CLUSTER PROPERTIES

In order to perform simulations of spectra with RS, we adopt a spherically-symmetric model of a cluster based on observations of the Perseus Cluster with *XMM-Newton* and *Chandra* to obtain the radial dependence of the electron number density, temperature and abundance of heavy elements. In particular, we use all available archival data from the EPIC-MOS CCD array on *XMM-Newton* with a total exposure $\sim$ 580 ks, and the *Chandra* ACIS-S observations with a total exposure $\sim$ 780 ks. Calibrated event lists from the *XMM* observations were generated using SAS version 12.0.1 (the details of the analysis are described by Churazov et al. 2003). The *Chandra* data are processed using the latest calibration data and following the algorithms developed by Vikhlinin et al. (2005). Fig. 1 shows the *Chandra* image of the Perseus Cluster.

Excluding point sources and a 12 arcsec region around the central AGN, the projected spectra in radial annuli are obtained. Fig. 2 shows the projected spectra from the 0.5-2 arcmin annulus. We fit the projected spectra with
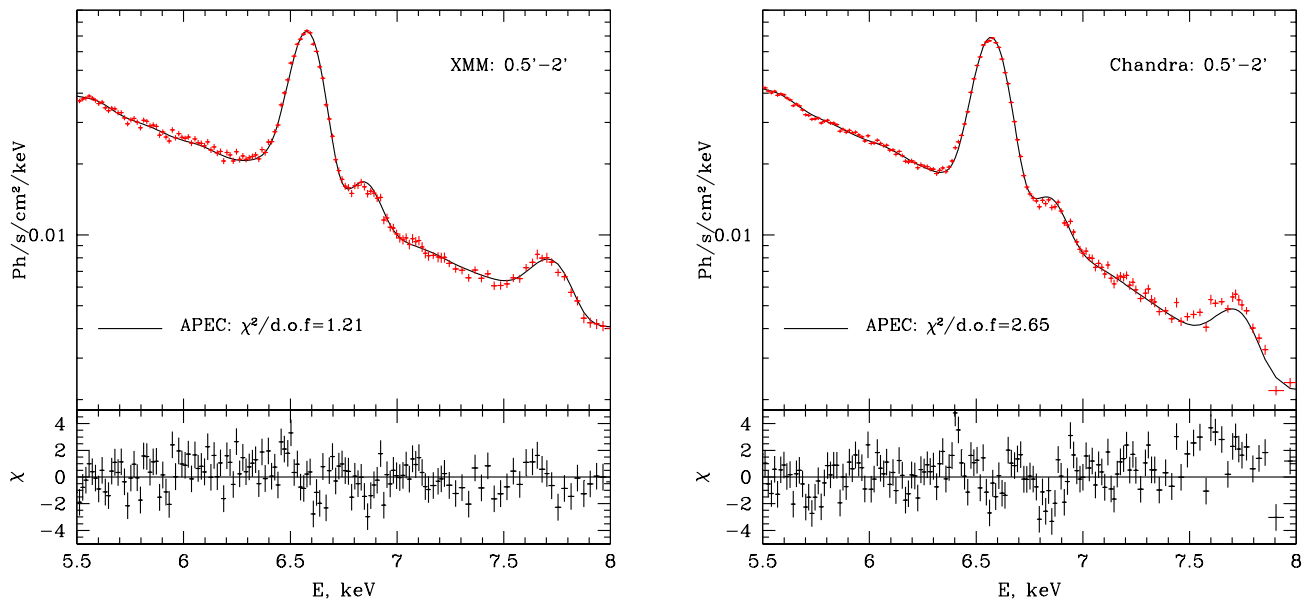
Figure 2. Projected spectra (red points) of the Perseus Cluster from the central 0.5-2 arcmin annulus obtained from the *XMM-Newton* (left) and *Chandra* (right) observations. In both the cases data is fitted by APEC model in 5-9 keV energy band (black curve). Residuals are shown in lower panels.

XSPEC (version 12.8.0) using 1T APEC plasma models with AtomDB version 2.0.1 (Smith et al. 2001; Foster et al. 2012) leaving temperature, metal abundance and redshift as free parameters. When fitting the spectra in a broad 0.5-9 keV band, the fit is poor, even if we use two-temperature (2T) plasma model. Reduced χ^2 and the best-fitting temperatures and abundances are shown in Table 1. This is not surprising, since the spectrum is multi-temperature both due to projection effects and due to the presence of the ICM with different temperatures at the same spatial distance from the cluster center. In order to avoid strong bias in the derived parameters, we restrict our analysis to the harder band 5-9 keV, where the role of cool gas is less significant. This band contains the 6.7 keV Fe line complex, where the RS is the strongest for Perseus. Fig. 2 shows the best-fitting 1T APEC models in the 5-9 keV band plotted on top of the observed data. Note, that in this band the 1T model represents data quite well. Table 1 shows the goodness of the best-fitting models (1T-model, 2T-model and a model with variable Ni abundance). Notice, that changing abundance to Lodders (2003), allowing for 2T plasma or varying Ni abundance do not give significant advantage over the 1T plasma models. χ^2 remains unchanged for the 5-9 keV band.

The success of the 1T APEC model with the *XMM-Newton* projected spectrum in the core of the cluster in the 5-9 keV band is particularly interesting. We do not see suppression in the K_α FeXXVI line complex due to the RS. This suggests that turbulent motions of gas are present in the core of Perseus. This conclusion is in agreement with previous findings of Molendi et al. (1998); Churazov et al. (2004); Tamura et al. (2009). However, comparing the *XMM-Newton* and *Chandra* spectra we see that the 1T APEC model visibly deviates from the *Chandra* spectrum near the 7.8 keV feature. We attribute this discrepancy to

the imperfect cross-calibration of both instruments[1]. Our experiments with various versions of the APEC code (version 1.3.1 – 2.0.1) show that differences of the order of few per cent are possible in the energy range of interest. The uncertainties in the plasma emission models, e.g., in the ionization balance, might give additional non-negligible contributions (Foster et al. 2012; Loewenstein & Davis 2012). While these small differences are typically unimportant, in the context of the RS effect they may play a role, since the expected line suppression in low resolution spectra is of the order of 10 per cent or smaller. At the same time, statistics of the spectra, accumulated by *Chandra* and *XMM-Newton* is sufficient to detect per cent level deviations from the model. These calibration uncertainties do not affect strongly the best-fitting parameters of the 1T APEC model.

The success of the 1T model in the 5-9 keV band motivated us to use this band[2] to build a 3D spherically-symmetric model for the Perseus Cluster by deprojecting observed spectra using the procedure described in Churazov et al. (2003). This model will be used to produce spectral models that account for the RS, turbulent motions of gas, radial variations of thermodynamic quantities and projection effects.
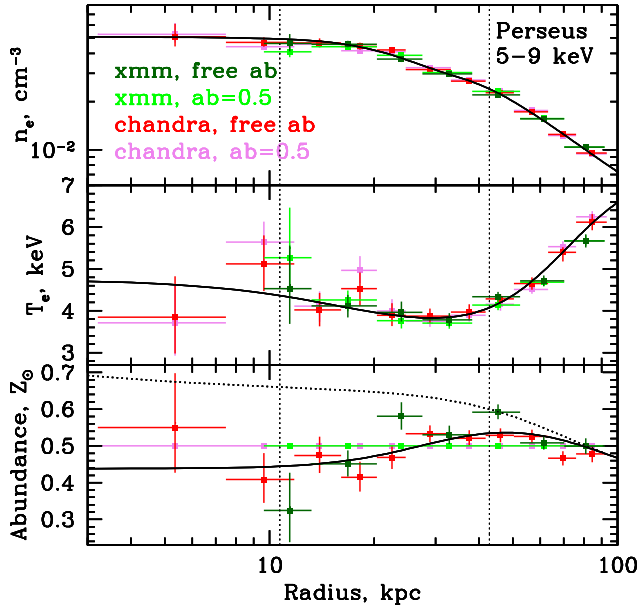
Deprojected profiles of electron number density, temperature and metal abundance are shown in Fig. 3. Results

---

[1] For instance, see the discussion of cross-calibration issues at the 8th IACHEC meeting in UK: http://web.mit.edu/iachec/meetings/

[2] We have checked that 1T APEC model in the broader 0.5-9 keV band still provides poor fit even to the deprojected spectra, although better than for the projected spectra. This indicates that at some level multi-temperature plasma is also present at the same 3D distance from the center.

Table 1. Goodness of the best-fitting models of optically thin plasma to the observed projected spectra in the 0.5-2 arcmin annulus in the Perseus Cluster. Spectra from the *XMM-Newton* and *Chandra* observatories are fitted in a broad 0.5-9 keV band and harder 5-9 keV band. χ^2 is shown for one-temperature APEC models assuming two difference tables of Solar abundances (A&G and Lodd respectively, Anders & Grevesse 1989; Lodders 2003), two-temperature APEC model and VAPEC with the Ni abundance as an additional free parameter. In the last model, metal abundances of all elements are tied except for the Ni. The best-fitting temperatures and abundances of Fe and Ni are also listed.

Model	0.5-9 keV					5-9 keV				
	T_1, keV	T_2, keV	$Z_{Fe}/Z_\odot$	$Z_{Ni}/Z_\odot$	χ^2/d.o.f. (d.o.f.)	T_1, keV	T_2, keV	$Z_{Fe}/Z_\odot$	$Z_{Ni}/Z_\odot$	χ^2/d.o.f. (d.o.f.)
XMM-Newton										
A&G, 1T	3.59	-	0.50	-	23.05 (561)	4.43	-	0.48	-	1.20 (261)
Lodd, 1T	3.96	-	0.9	-	35.14 (561)	4.37	-	0.72	-	1.19 (261)
2T	2.17	5.01	0.45	-	13.77 (559)	4.3	64.0	0.48	-	1.18 (259)
vapec, Ni	3.59	-	0.51	0.86	22.9 (560)	4.47	-	0.50	0.59	1.20 (260)
Chandra										
A&G, 1T	3.58	-	0.52	-	75.42 (577)	4.33	-	0.47	-	2.65 (269)
Lodd, 1T	4.01	-	0.99	-	59.4 (577)	4.31	-	0.72	-	2.51 (269)
2T	5.23	2.17	0.44	-	53.37 (575)	3.45	22.5	0.58	-	2.60 (267)
vapec, Ni	3.57	-	0.51	0	74.12 (576)	4.30	-	0.47	1.02	2.49 (268)

Figure 3. Deprojected number density of electrons (top), gas temperature (middle) and abundance of heavy elements (bottom) in the Perseus Cluster obtained from the *Chandra* and *XMM-Newton* observations in the $5-9$ keV energy band. Profiles were obtained while treating abundance of heavy elements both as a free parameter and fixing it to a constant value 0.5 relative to solar. Black solid curves show the approximation used as an input for our calculations of resonant scattering models. The dotted black curve shows the "peaked-in-the-core" metal abundance radial profile. Parametric fits are given in Appendix A. Vertical dotted lines across all panels indicate 0.5-2 arcmin region.

from both observatories are consistent with each other although the scatter in T and Z increases toward the cluster core. As starting values we use the redshift $z = 0.0176$ of

the central galaxy NGC1275 from NED[3] and N_H column density $1.38 \cdot 10^{21}$ cm^{-2} in the core of the cluster (Kalberla et al. 2005; Dickey & Lockman 1990). N_H is fixed, but the redshift is allowed to vary. Given extremely high statistics, even very small variations of the redshift, at the level of $\Delta z \sim 10^{-3}$ would cause visible residuals in the spectra. The best-fitting values of the redshift for the 1T APEC models are 0.0152 and 0.0167 for *XMM-Newton* and *Chandra*, respectively. We assume that these variations are within calibration uncertainties and use the best-fitting values. The observed profiles are approximated with the smooth functions shown with black curves in Fig. 3.

Deprojected spectra were fitted with 1T APEC plasma model assuming either constant metal abundance of 0.5 solar relative to Anders & Grevesse (1989), or leaving abundance as a free parameter of the model. In terms of density and temperature profiles the assumption of constant or variable abundance does not have strong impact. We therefore can fix the density and temperature profiles and consider several different models of the abundance radial profile. Contrary to expectations of the highest abundance of heavy elements in the very core of the cluster due to the presence of the massive elliptical galaxy NGC1275, we see a drop of abundance in the core of Perseus, broadly discussed in the literature (see, e.g., Schmidt, Fabian, & Sanders 2002; Churazov et al. 2003). Similar drops are observed in other clusters and are (at least in some systems) attributed to the use of oversimplified spectral models in the presence of several temperature components (e.g., Buote & Fabian 1998; Werner et al. 2008). RS can also be responsible for the apparent drop of the abundance in the cluster core. However, neither of these explanations seems to be sufficient to fully explain the metal abundance dip in the core of Perseus (see Sanders et al. 2004; Sanders & Fabian 2006; Churazov et al. 2004; Tamura

[3] http://ned.ipac.caltech.edu/

et al. 2009). Given that the RS effect could contribute to the drop of the abundance, we also perform simulations using a "peaked" abundance profile (black dotted curve in Fig. 3) in the core. This "peaked" profile was selected to approximately compensate the suppression of the resonant line flux by the RS (see Section 4.2). Functional forms of n_e, T and Z are presented in Appendix A.

3 RADIATIVE TRANSFER SIMULATIONS

The radiative transfer code developed for this work produces projected spectra accounting for (i) the RS effect, (ii) radial variations of density/temperature/abundance in clusters and (iii) line broadening due to the turbulent motions of gas. The code is based on earlier simulations discussed in Sazonov, Churazov, & Sunyaev (2002) and Zhuravleva et al. (2010, 2011). The key feature of our code is the self-consistent treatment of the whole spectrum in the radiative transfer calculations. The output is in the same format of XSPEC models and allows one to directly compare the models with observed data in a usual way. Below we briefly describe the code.

Once we have a cluster model (see Section 2), the spectrum emitted by each spherical shell is calculated. The line emissivity, continuum and pseudo continuum are taken from APEC (AtomDB version 2.0.1) code (Smith et al. 2001; Foster et al. 2012). The continuum in APEC includes bremsstrahlung, radiative recombination and two photon emission, while pseudo continuum takes into account all weak lines which are not included in the emissivity files. Both the lines and continuum associated with a given element are convolved with a Gaussian, to account for the line broadening. The Gaussian velocity width is determined both by thermal broadening and broadening due to small-scale isotropic gas motions, as parameterized through the Mach number[4] M

$$\sigma = \frac{E_0}{\sqrt{2}} \left(\frac{2kT_e}{Am_p c^2} + M^2 \right)^{1/2}. \tag{1}$$

Here E_0 is the rest energy of the line, A is the atomic mass of the corresponding element, m_p is the proton mass. Line broadening due to radiative decay of levels is neglected. We use the definitions of solar abundances of Anders & Grevesse (1989). The ionization balance (collisional equilibrium) is taken from Mazzotta et al. (1998).

The optical depth from the center to the edge of cluster at the center of a line is defined as

$$\tau = \int_0^\infty \frac{\sqrt{2\pi} h r_e c f}{\sigma} n_p Z \delta_i dr, \tag{2}$$

where h is the Planck constant, r_e is the classical radius of an electron, f is the oscillator strength of a transition, n_p is the number density of protons, Z is the abundance of a given element relative to hydrogen and δ_i is the fraction of the elements in the appropriate ionization state. The optical depth in continuum is calculated through the Thomson cross section as follows
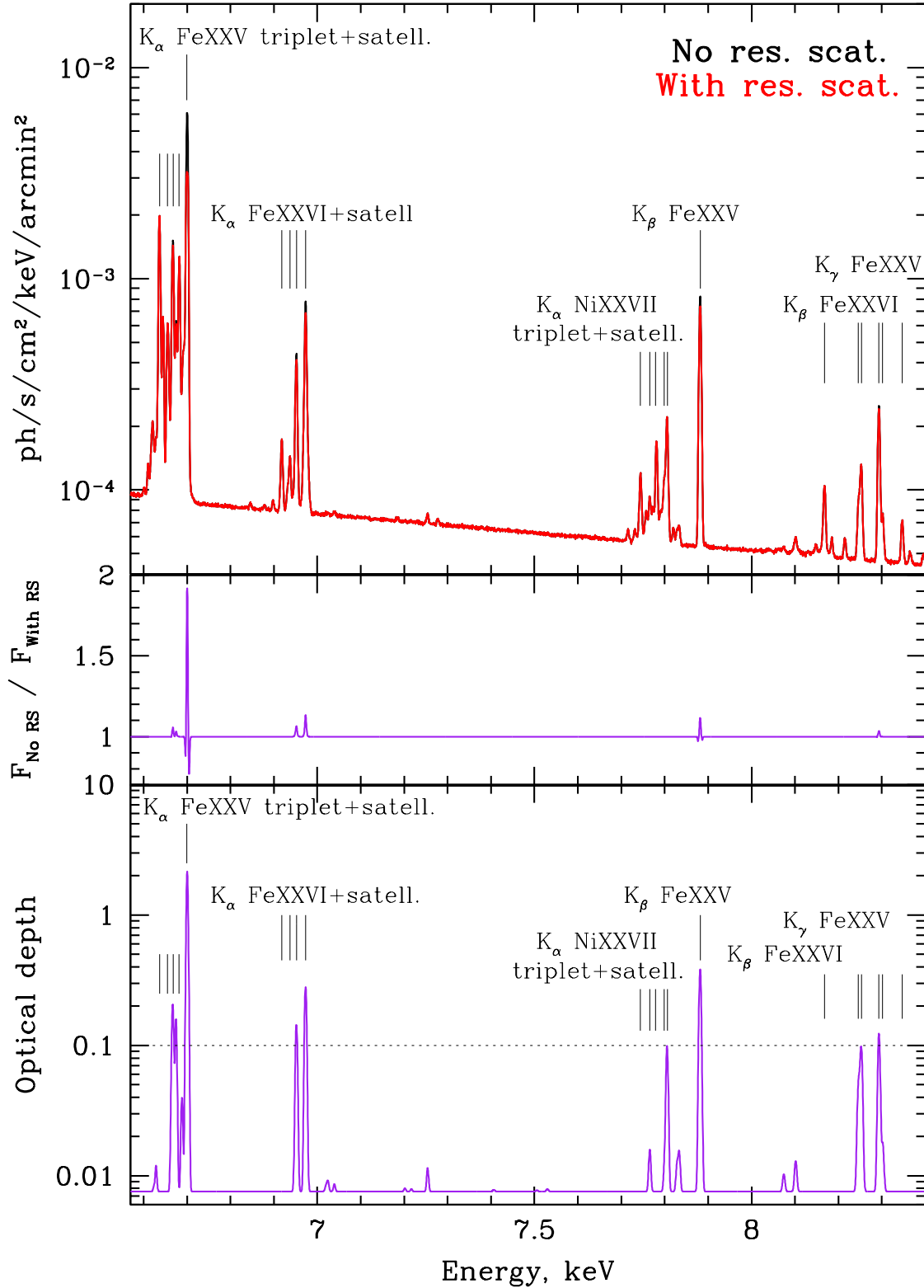
$$\tau = \int_0^\infty \sigma_T r_e^2 n_e dr. \tag{3}$$

The scattering loop starts by drawing not only initial position and direction of photon propagation, but also its energy. The photon has initially a unit weight w that reduces after each scattering by a factor $(1 - e^{-\tau})$, where τ is the optical depth in the direction of photon propagation. At the same time the quantity $w \cdot e^{-\tau}$ is added to an appropriate bin (set by the energy and the projected distance of the photon) of the emergent spectra. The scattering process repeats until the weight drops below the set minimal value w_{min}, which in our case is $w_{min} = 10^{-6}$. During each scattering, the new position of the emerging photon and the new direction are drawn in accordance with the isotropic scattering phase matrix (the use of Rayleigh phase function does not affect the results significantly unless polarization is taken into account). The photon energy after the scattering is $E = E_0 \left(1 + \frac{(\mathbf{V_{ion}}\mathbf{m'})}{c} \right)$, where $\mathbf{V_{ion}}$ is the velocity of the scattering ion, $\mathbf{m'}$ is the new direction of photon propagation and E_0 is the line energy. The ion velocity in the direction of photon propagation is $V_{ion,||} = c(1 - E_0/E)$, so that the photon energy in the reference frame of the ion is equal to E_0 and scattering occurs. Other ion velocity components have Gaussian distribution with the width set by the Doppler line width.

Since we consider scattering of photons in a certain energy band, a large number of photons n_{ph} is required in order to produce statistically robust results (e.g., we use $n_{ph} = 10^9$ for simulations in 4-10 keV band). Such calculations are time consuming, although straightforward parallelisation of the Monte Carlo simulations can address this problem. Additionally, we introduce a threshold in the optical depth τ_{min} of individual lines. Only lines with $\tau > \tau_{min} = 0.1$ participate in the scattering process. To ensure good statistics over the whole range of radii, a radially dependent weight is used to draw positions of emitted photons. This allows one to reach robust results using reasonable total number of photons. We refer the reader to our previous works (Sazonov, Churazov, & Sunyaev 2002; Zhuravleva et al. 2010, 2011) for more details on how the scattering process is modeled in the simulations.

4 RESULTS

### 4.1 Spectral models of RS in Perseus

Fig. 4 and 5 show the results of our simulations. We show the spectrum only for the 0.5-2 arcmin annulus (see Fig. 1), where line suppression due to RS is expected to be the

---

[4] The Mach number is determined as a ratio of the characteristic velocity of turbulence and the adiabatic sound speed, $M = V_{\rm turb}/c_s$. Note, that in the code $V_{\rm turb} \equiv \sqrt{2} V_{\rm 1D,turb}$, where $V_{1D,turb}$ is the velocity dispersion along the line of sight. Coefficient $\sqrt{2}$ is chosen to be consistent with definitions from our previous works.

Figure 4. Predicted spectrum of the Perseus Cluster, which takes into account distortions of the line's flux and shape induced by resonant scattering. **Top:** projected spectra from the 0.5 - 2 arcmin annulus (see Fig. 1) both with (red) and without (black) the scattering. **Middle:** ratio of spectral models without and with resonant scattering. **Bottom:** optical depth as a function of energy. Only lines with the optical depths above the threshold $\tau = 0.1$ (dotted line) are involved in the scattering process. The strongest lines are labeled and their characteristics are shown in Table 2.

Table 2. The strongest lines marked in Fig. 4 and Fig. 5: their energy, transition information (level notations are according to APEC), and the radial optical depth calculated at the center of line assuming two different metal abundance models.

Ion	Energy, keV	Upper level	Lower level	Transition			$\tau(M=0)$ "free" ab. eq. (A3)	$\tau(M=0)$ "peaked" ab. eq. (A4)	Comments
FeXXV	8.347	10192	3	$1s2s(^1S_0)$	-		0.0e0	0.0e0	satellite
FeXXV	8.302	21	1	$1s^2(^1S_0)$	-	$1s4p(^3P_1)$	9.3e-3	1.2e-2	He-like K_γ, intercomb.
FeXXV	8.293	23	1	$1s^2(^1S_0)$	-	$1s4p(^1P_1)$	1.1e-1	1.3e-1	He-like K_γ, reson.
FeXXVI	8.253	7	1	$1s(^2S_{1/2})$	-	$3p(^2P_{3/2})$	8.3e-2	9.7e-2	H-like K_β
FeXXVI	8.246	6	1	$1s(^2S_{1/2})$	-	$3p(^2P_{1/2})$	4.1e-2	4.8e-2	H-like K_β
FeXXV	8.168	10127	3	$1s2s(^1S_0)$	-		0.0e0	0.0e0	satellite
FeXXV	7.882	11	1	$1s^2(^1S_0)$	-	$1s3p(^3P_1)$	2.8e-2	3.4e-2	He-like K_β , intercomb.
NiXXVII	7.806	7	1	$1s^2(^1S_0)$	-	$1s2p(^1P_1)$	7.1e-2	8.8e-2	He-like K_α, reson.
NiXXVII	7.799	6	1	$1s^2(^1S_0)$	-	$1s2p(^3P_2)$	2.3e-6	2.8e-6	He-like K_α, intercomb.
NiXXVII	7.779	10001	1	$1s^2(^1S_0)$	-		0.0e0	0.0e0	satellite
NiXXVII	7.766	5	1	$1s^2(^1S_0)$	-	$1s2p(^3P_1)$	7.7e-3	9.4e-3	He-like K_α , intercomb.
NiXXVII	7.744	2	1	$1s^2(^1S_0)$	-	$1s2s(^3S_1)$	4.9e-8	6.0e-8	He-like K_α, forbid.
FeXXVI	6.973	4	1	$1s(^2S_{1/2})$	-	$2p(^2P_{3/2})$	2.6e-1	3.0e-1	H-like K_α
FeXXVI	6.952	3	1	$1s(^2S_{1/2})$	-	$2p(^2P_{1/2})$	1.3e-1	1.5e-1	H-like K_α
FeXXVI	6.937	10017	6	$3p(^2P_{1/2})$	-		0.0e0	0.0e0	satellite
FeXXVI	6.918	10004	2	$2s(^2S_{1/2})$	-		0.0e0	0.0e0	satellite
FeXXV	6.700	7	1	$1s^2(^1S_0)$	-	$1s2p(^1P_1)$	1.98e0	2.5e0	He-like K_α, reson.
FeXXV	6.682	6	1	$1s^2(^1S_0)$	-	$1s2p(^3P_2)$	4.6e-5	5.7e-5	He-like K_α, intercomb.
FeXXV	6.668	5	1	$1s^2(^1S_0)$	-	$1s2p(^3P_1)$	1.6e-1	2.0e-1	He-like K_α, intercomb.
FeXXV	6.655	10076	6	$1s2p(^3P_2)$	-		0.0e0	0.0e0	satellite
FeXXV	6.637	2	1	$1s^2(^1S_0)$	-	$1s2s(^3S_1)$	8.4e-7	1.0e-6	He-like K_α, forbid.
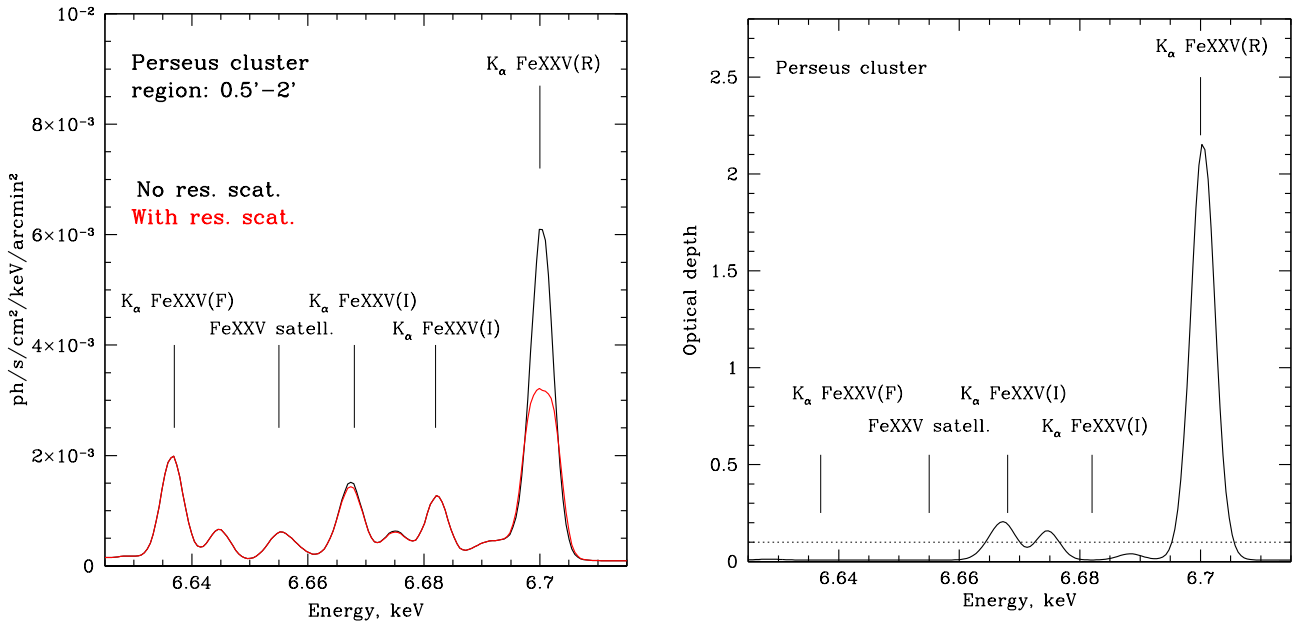
Figure 5. Resonant scattering effect in the He-like Fe triplet in the Perseus Cluster. See Fig. 4 and Table 2.

strongest in the Perseus Cluster (for more details see Churazov et al. 2004). The central 0.5 arcmin region is excluded from the analysis since there is a significant central AGN contribution. The top panel in Fig. 4 shows model spectra with and without the RS. The corresponding optical depth as a function of energy is shown in the bottom panel. No-

tice, that several lines in the 6.5-8.4 keV band are affected by scattering. Seven lines have the optical depth $\tau > 0.1$, while the line of the He-like iron (K_α FeXXV with the rest energy 6.7 keV) has the highest optical depth $\tau \sim 2$. Fig. 5 shows the same model spectra and optical depths in closeup in the region at the He-like Fe line. Table 2 lists the line
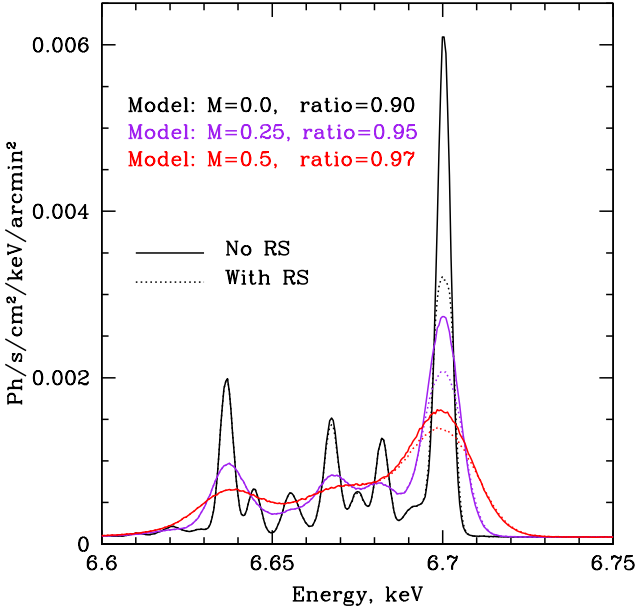
Figure 6. Predicted spectrum of the Perseus Cluster (from 0.5-2 arcmin annulus) with and without resonant scattering and different levels of gas turbulence. The He-like Fe triplet line complex is shown for the Mach numbers 0, 0.25 and 0.5. Solid: no resonant scattering, dotted: with resonant scattering. The ratio of fluxes with and without scattering integrated over 6.6-6.75 keV band is shown in the left corner. As expected, the higher the velocity of the turbulent motions of gas, the broader lines and the weaker line distortions due to the resonant scattering.

energy, transition information and the radial optical depth for the strongest lines obtained assuming "free" metal abundance (eq. A3) and "peaked" (eq. A4) abundance models. As expected, the larger the optical depth, the stronger the line suppression due to the RS. For the K_α FeXXV line at 6.7 keV, the suppression is ~ 25 per cent. Two other lines of K_β FeXXV and K_α FeXXVI with the optical depths ~ 0.4 and ~ 0.3, respectively, have a line flux suppression of ~ 5 per cent.

Varying the level of turbulence through the Mach number, we produce models that can be used to constrain the amplitude of turbulent motions. Fig. 6 shows the spectral models in the 6.7 keV region obtained for the Mach numbers 0, 0.25 and 0.5. The higher the turbulence, the less prominent the RS and the broader lines are. Integrating fluxes with and without scattering over the line complex around 6.7 keV, we see that the suppression of the total flux of the 6.7 keV complex decreases from 10 per cent at $M = 0$ down to 3 per cent at $M = 0.5$.

In order to simplify the comparison of our models with observed data, we have tabulated model spectra in the XSPEC format[5].

---

[5] Models for the Perseus Cluster and brief description of how to use them can be downloaded at http://www.mpa-garching.mpg.de/∼izhur/rs_models_perseus/

4.2 Comparison with existing data

Below we compare our models with the existing *XMM-Newton* data on the Perseus Cluster. By default we compare data with models that have zero Mach number (no gas motions), unless other model is specified.

We use the projected spectrum from the 0.5-2 arcmin annulus, which is plotted with red points in Fig. 7. The energy resolution of *XMM* is insufficient to resolve individual lines seen in the theoretical models (c.f. Fig. 4). Instead, we see three bumps, which contain complexes of lines: the K_α FeXXV complex around 6.7 keV (redshifted to ~ 6.6 keV), the K_α FeXXVI complex at 6.97 keV (redshifted to ~ 6.85 keV), and the K_β FeXXV with K_α NiXXVII line complexes around 7.85 keV (redshifted to ~ 7.7 keV).

Given the uncertainty in the metal abundance profiles, we have calculated two models assuming "free" and "peaked" abundance of heavy elements (see Section 2). Models, convolved with the *XMM-Newton* response are shown with the black curves on top of the observed points in Fig. 7. When doing the comparison of the predicted and observed spectra, we do rudimentary correction of the normalization (within 1-2 per cent) and the redshift (less than 10^{-3}) to ensure that the comparison is dominated by the flux ratio of different lines rather than by the difference in the observed and adopted values of the redshift and density normalization. The "free" abundance model (left panel) represents our best efforts to describe radial variations of the observed metal abundance profile (derived from 1T fits of deprojected spectra in the 5-9 keV band) under the assumption of optically thin plasma. Notice, that in this case the model *without* the RS describes data the best. The χ^2 is reasonable, given the simplicity of the model. It is only slightly higher than direct fitting of the projected spectrum with the 1T APEC model. The fact that the 1T APEC model marginally wins over our model is not entirely surprising, since deprojected profiles are designed to reproduce overall structure of the cluster, rather than the projected spectrum in this particular annulus. The model with RS predicts a line flux value well below the measured one (dotted curve in the left panel of Fig. 7). In contrast, the "peaked" abundance model is the result of several trials to find a radial metal abundance profile, for which the model *with* the RS predicts a 6.7 keV line flux broadly compatible with the data (the right panel). Indeed, we see that in this case the model without the RS predicts significantly higher flux at the 6.7 keV line complex. The "peaked" model is also driven by the desire to have the abundance rising towards the center, rather declining, like in the "free" abundance model. To this end, the "peaked" model is one of the possible models and is not necessarily the very best one in terms of χ^2. Nevertheless, our "peaked" model gives χ^2 just slightly higher than the case of "free" metal abundance.

Comparison of our models with the *Chandra* data of the Perseus Cluster gives higher χ^2 than for the *XMM-Newton* data. This is due to stronger deviations of the Ni-line complex from the model, as discussed in Section 2. In the case of "free" abundance model, χ^2/d.o.f. is 2.87 (d.o.f.=271) and 5.48 (271) for models without and with the RS, respectively.
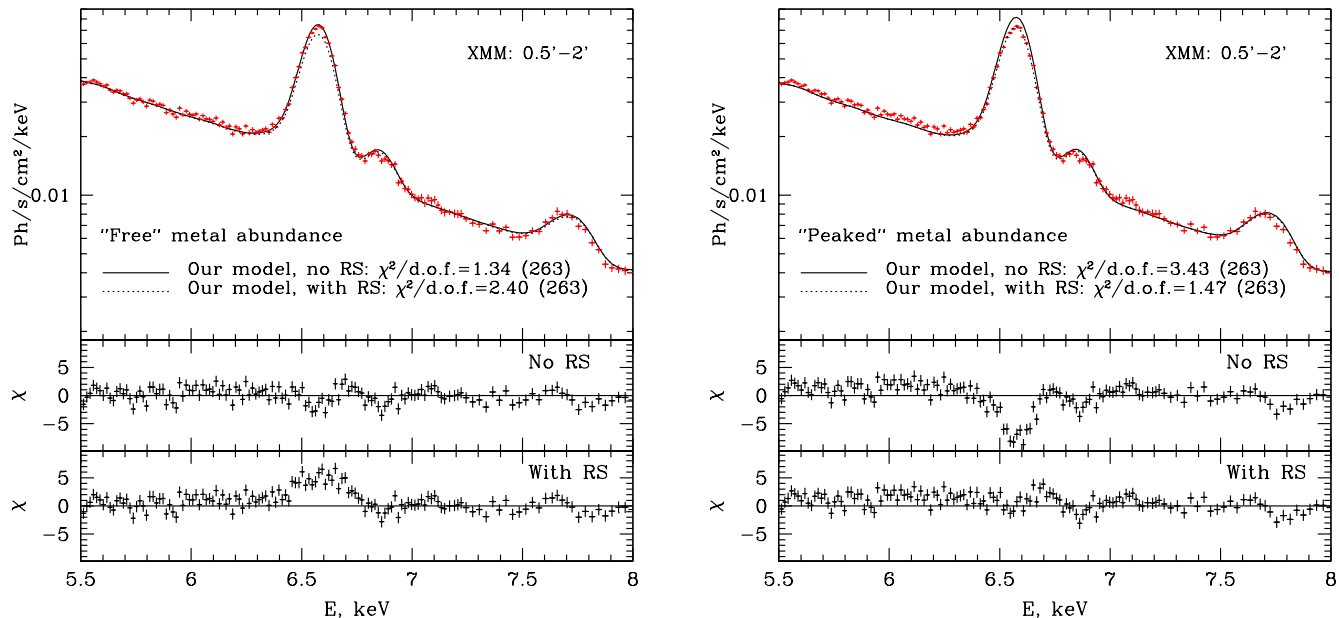
Figure 7. Comparison of our models with the *XMM-Newton* projected spectrum of the Perseus Cluster. Red points show the observed projected spectra from the central 0.5-2 arcmin annulus obtained from the *XMM-Newton* observations. Our spectral models are shown with black curves. Solid/dotted curves correspond to the cases without/with resonant scattering. Deviations of our models from the observed data are shown in the lower panels. Here, we show models without turbulent motions of gas, the Mach number $M = 0$. χ^2 per d.o.f. are labeled with a number of d.o.f. in brackets. **Left:** *XMM* data and our model with a "free" abundance of heavy elements (eq. A3). As can be seen from the figure, deviations of the model *with* resonant scattering are significantly stronger around 6.7 keV line complex. **Right:** *XMM* data and results of our simulations with "peaked" metal abundance (eq. A4). Notice, that the energy resolution of current X-ray observatories does not allow us to separate spectral modifications due to different metal abundance and presence of the resonant scattering (see Fig. 8 for more details).

For the "peaked" abundance, χ^2/d.o.f. is 6.55 (271) and 2.90 (271) correspondingly.

Fig. 8 compares the "best-fitting" models discussed above to model with "free" metal abundance and turbulent motions of the gas with Mach number M=0.5 (the left panel). We see that all three models are barely distinguishable. The spectral resolution of the *XMM-Newton* (and *Chandra*) observatory is not sufficient to robustly separate spectral distortions induced by the RS, different metal abundance profiles and different levels of the gas turbulence. The situation changes dramatically if we have *Astro-H* energy resolution ~ 5 eV. The right panel shows how differently spectra look if we vary the abundance profile, presence/absence of the RS and the level of turbulence. Notice, that with the *Astro-H* data we would be able to distinguish different models and make conclusion on the RS effect in Perseus even using a narrow energy band around the 6.7 keV line complex.

4.3 Future prospects with *Astro-H*

A new era of X-ray spectroscopy employing X-ray calorimetry will start with the launch of Japanese mission *Astro-H*[6] (see e.g. Takahashi et al. 2010). The Soft X-ray Spectrometer (SXS) system on-board of *Astro-H* will have an energy resolution ~ 5 eV between 0.3-10 keV, which is ~ 30 times better than the energy resolution around 6.7 keV line of the current X-ray CCDs. Such high spectral resolution is enough to resolve individual lines in spectra of galaxy clusters. It will allows us to resolve the degeneracy between "peaked abundance - RS" and "free abundance - no RS" problem, mentioned in the previous Section. Also, looking at individual lines, the existing plasma models can be tested in great detail.

The effect of the RS in the core of the Perseus Cluster will be readily seen already with 100 ks observations. Fig. 9 shows simulated spectra from the 0.5-1.5 arcmin annulus in Perseus as *Astro-H* will measure with a 100 ks pointing observation. We used the whole field of view, 2.85 arcmin on a side, with excluded central chip, where the contribu-

---

[6] http://astro-h.isas.jaxa.jp/
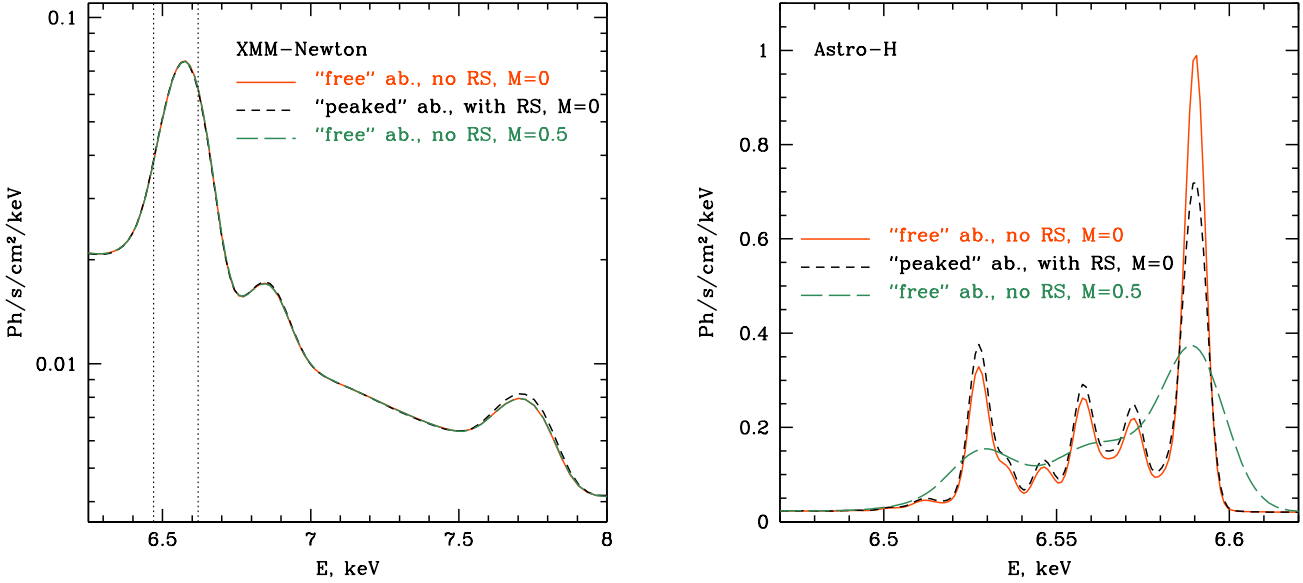
Figure 8. Sensitivity of predicted spectra convolved with response matrices of the *XMM-Newton* (left) and *Astro-H* (right) observatories to the heavy elements abundance, the level of gas turbulence and presence of resonant scattering in the Perseus Cluster. The spectra for the 0.5-2 arcmin annulus are shown. Note, that the energy resolution of current X-ray instruments is not sufficient for resolving individual lines. Therefore, spectral distortions due to the resonant scattering, different metal abundance profiles and different level of gas turbulence are able to compensate each other in the final spectrum. In contrast, energy resolution of *Astro-H* is sufficient to detect and separate spectral distortions of different origin. Even a very narrow spectral region around 6.7 keV line (also indicated with a vertical dotted line in the left panel) allows us to do it.

tion of the central AGN is dominating the signal. The RMF and ARF files were taken from http://astro-h.isas.jaxa.jp/. We used the SXS energy response assuming constant energy resolution of 5 eV, while the ARF for all pixels was taken for point sources with open filter. Simulations neglect the redistribution of photons due to the mirror point-spread-function. Points show simulated spectra with and without RS for Mach numbers 0 and 0.5, while solid curves show our models, convolved with the *Astro-H* response. Notice, even if the level of turbulence is high (M=0.5), *Astro-H* will be easily capable of measuring the suppression of lines. Here we assumed only statistical uncertainties. The next step will be to perform more realistic simulations of the spectra in the Perseus Cluster, accounting for mirror blurring and the finite pixel size of the detector (Konami et al. 2013, in prep.).

Note that the above model was produced assuming small-scale gas motions. In this context small-scale means scales much smaller than the characteristic size of the Perseus Cluster core. This implies that a Gaussian is a good description of the line profile. When large scale motions are present the line shape may have a complicated shape dominated by stochastic velocity fields (Zhuravleva et al. 2012; Shang & Oh 2012). Useful approaches for studying such cases may include the use of optically thin lines to infer template line shapes or the approaches developed by Shang & Oh (2012). Note that the amplitude of the RS effect depends on the dominant anisotropy in the velocity field (Zhuravleva et al. 2011). It should be possible therefore to test if the line broadening/shape and the line ratios are self-consistent.

5 CONCLUSIONS

We have produced spectral models for the Perseus Cluster which take into account modifications of line fluxes and shapes due to the RS effect, line broadening by small-scale motions and radial variations of density, temperature and abundance of heavy elements. Similar calculations can be easily extended for any spherically-symmetric model of other clusters. The main advantage of the model is that it self-consistently accounts for projection effects, line broadening and scattering of photons produced not only for a single line, but for the whole spectrum at once. This is particularly important when line broadening causes overlap of individual lines. Our models can be directly compared to data in a certain energy band, accounting for the suppression of all optically thick lines in this band. This provides more robust constraints on the RS and the amplitude of gas motions in clusters. The model spectra are stored in the XSPEC format and can be used straightforwardly in a usual way.

We have compared our model to the existing data of the Perseus Cluster from the *Chandra* and *XMM-Newton* observatories. We do not see strong evidence for the RS in the central 0.5-2 arcmin region. However, we showed that a firm conclusion on the presence or absence of the RS cannot be easily made with existing data since the limited energy resolution of the spectra complicates model comparisons. Spectral models convolved with the CCD resolution are largely degenerate if we vary the metal abundance profile and/or the Mach number. With the current data one has to rely on the comparison of line fluxes from different ions or elements.

The high energy resolution of the future X-ray observa-
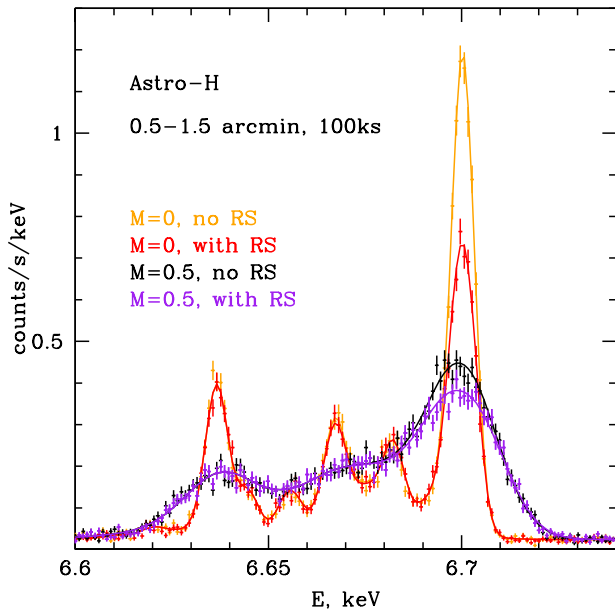
Figure 9. Simulated spectra from the core (0.5-1.5 arcmin annulus) of the Perseus Cluster as *Astro-H* will obtain from 100 ks pointing observation. We used the whole field of view (2.85 arcmin on a side) with excluded central chip, where the contribution of the central AGN is dominating the signal. Points show the "observed" spectra (only statistical uncertainties are included), while solid curves show model spectra without and with resonant scattering respectively. Notice, that 100 ks observation is enough to detect the resonant scattering signal even if motions of gas are present.

tory *Astro-H* should enable us to resolve most of the problems we are facing with the current data. The abundance of heavy elements will be better constrained since we will see individual lines of the same ions in spectra. Calculations of the line emissivities using APEC models of optically thin plasma (or any other plasma emission code) will be tested on resolved optically thin lines in spectra from the *Astro-H* observations. Modifications in spectra due to the presence of turbulence will be easy to detect. Therefore, analysis of the RS effect can be done self-consistently with the help of models presented in this work. We have shown that 100 ks observations will be enough to make a significant step forward in the RS measurements.

6   ACKNOWLEDGEMENTS

REFERENCES

Akimoto F., Furuzawa A., Tawara Y., Yamashita K., 1999, AN, 320, 283

Anders E., Grevesse N., 1989, GeCoA, 53, 197
Arnaud K. A., 1996, ASPC, 101, 17
Bulbul G. E., Smith R. K., Foster A., Cottam J., Loewenstein M., Mushotzky R., Shafer R., 2012, ApJ, 747, 32
Buote D. A., Fabian A. C., 1998, MNRAS, 296, 977
Churazov E., Forman W., Jones C., Böhringer H., 2003, ApJ, 590, 225
Churazov E., Forman W., Jones C., Sunyaev R., Böhringer H., 2004, MNRAS, 347, 29
Churazov E., Zhuravleva I., Sazonov S., Sunyaev R., 2010, SSRv, 157, 193
de Plaa J., Zhuravleva I., Werner N., Kaastra J. S., Churazov E., Smith R. K., Raassen A. J. J., Grange Y. G., 2012, A&A, 539, A34
Dickey J. M., Lockman F. J., 1990, ARA&A, 28, 215
Dupke R. A., Arnaud K. A., 2001, ApJ, 548, 141
Ezawa H., et al., 2001, PASJ, 53, 595
Foster A. R., Ji L., Smith R. K., Brickhouse N. S., 2012, ApJ, 756, 128
Gastaldello F., Molendi S., 2004, ApJ, 600, 670
Gilfanov M. R., Syunyaev R. A., Churazov E. M., 1987, SvAL, 13, 3
Kahn S. M., et al., 2003, ASPC, 301, 23
Kalberla P. M. W., Burton W. B., Hartmann D., Arnal E. M., Bajaja E., Morras R., Pöppel W. G. L., 2005, A&A, 440, 775
Lodders K., 2003, ApJ, 591, 1220
Loewenstein M., Davis D. S., 2012, ApJ, 757, 121
Mazzotta P., Mazzitelli G., Colafrancesco S., Vittorio N., 1998, A&AS, 133, 403
Molendi S., Matt G., Antonelli L. A., Fiore F., Fusco-Femiano R., Kaastra J., Maccarone M. C., Perola C., 1998, ApJ, 499, 608
Sanders J. S., Fabian A. C., 2006, MNRAS, 370, 63
Sanders J. S., Fabian A. C., 2013, MNRAS, 429, 2727
Sanders J. S., Fabian A. C., Allen S. W., Schmidt R. W., 2004, MNRAS, 349, 952
Sanders J. S., Fabian A. C., Smith R. K., 2011, MNRAS, 410, 1797
Sazonov S. Y., Churazov E. M., Sunyaev R. A., 2002, MNRAS, 333, 191
Schmidt R. W., Fabian A. C., Sanders J. S., 2002, MNRAS, 337, 71
Shang C., Oh S. P., 2012, MNRAS, 426, 3435
Shigeyama T., 1998, ApJ, 497, 587
Smith R. K., Brickhouse N. S., Liedahl D. A., Raymond J. C., 2001, ApJ, 556, L91
Takahashi T., et al., 2010, SPIE, 7732
Tamura T., et al., 2009, ApJ, 705, L62
Vikhlinin A., Markevitch M., Murray S. S., Jones C., Forman W., Van Speybroeck L., 2005, ApJ, 628, 655
Werner N., Durret F., Ohashi T., Schindler S., Wiersma R. P. C., 2008, SSRv, 134, 337
Werner N., Zhuravleva I., Churazov E., Simionescu A., Allen S. W., Forman W., Jones C., Kaastra J. S., 2009, MNRAS, 398, 23
Xu H., et al., 2002, ApJ, 579, 600
Zhuravleva I., Churazov E., Kravtsov A., Sunyaev R., 2012, MNRAS, 422, 2712

Zhuravleva I. V., Churazov E. M., Sazonov S. Y., Sunyaev
R. A., Dolag K., 2011, AstL, 37, 141

Zhuravleva I. V., Churazov E. M., Sazonov S. Y., Sunyaev
R. A., Forman W., Dolag K., 2010, MNRAS, 403, 129

APPENDIX A: SPHERICALLY-SYMMETRIC MODEL OF THE PERSEUS CLUSTER

Below we summarize our model of the Perseus Cluster used as an input to our simulations of spectra with RS (see Fig. 3). The number electron density $[\text{cm}^{-3}]$ radial profile is

$$
\begin{aligned}
n_e = &\left[\frac{4.6 \cdot 10^{-2}}{\left(1 + \left(\frac{r}{55}\right)^2\right)^{1.8}} + \frac{4.8 \cdot 10^{-3}}{\left(1 + \left(\frac{r}{200}\right)^2\right)^{0.87}} \right] \times \\
&\times \left[1 - 0.06 \exp\left(-\left(\frac{r-30}{9}\right)^2 \right) \right] \times \\
&\times \left[1 + 0.04 \exp\left(-\left(\frac{r-15}{8}\right)^2 \right) \right] ,
\end{aligned} \tag{A1}
$$

where r is in kpc. The profile of temperature [keV] is

$$
T_e = 7.5 \frac{1 + \left(\frac{r}{58}\right)^{3.5}}{2.45 + \left(\frac{r}{58}\right)^{3.6}} \times \frac{1.55 + \left(\frac{r}{20}\right)^{2.04}}{1 + \left(\frac{r}{20}\right)^2}. \tag{A2}
$$

"Free" metal abundance profile (relative to $Z_\odot$) is

$$
Z = 0.33 \frac{2 + 1.1 \left(\frac{r}{90}\right)^{2.7}}{1.1 + \left(\frac{r}{90}\right)^{2.7}} \times \frac{0.73 + \left(\frac{r}{30}\right)^3}{1 + \left(\frac{r}{30}\right)^3}, \tag{A3}
$$

while "peaked" abundance is assumed the following

$$
Z = 0.355 \frac{2 + 1.1 \left(\frac{r}{70}\right)^{2.7}}{1.1 + \left(\frac{r}{70}\right)^{2.7}} \times \frac{1 + \left(\frac{r}{1.5}\right)}{0.8 + \left(\frac{r}{1.5}\right)}. \tag{A4}
$$